Initiation and propagation of curved reaction front in solids: insights into solid combustion and battery thermal runaway

Peng Zhao[1]*, Antonio García[2], Tristan Burton[3]

[1]Department of Mechanical, Aerospace & Biomedical Engineering, UT Space Institute, University of Tennessee, Knoxville, Tennessee 37388, USA

[2]CMT – Motores Térmicos, Universitat Politècnica de València, Camino de Vera s/n, 46022 Valencia, Spain

[3]Convergent Science Inc., USA

*Corresponding author email: pzhao12@utk.edu

Abstract

As decarbonization and carbon neutrality become increasingly important, battery research has received more and more attention. One of the great challenges in battery is thermal runaway and its propagation, which is fundamentally a combustion problem featured by reaction-conduction coupling, with negligible effects from mass diffusion in the time scale of interest. In this work, a large Ze number asymptotic analysis was performed to describe spherical and cylindrical reaction front initiation and propagation in solid combustion, assuming one-step global chemistry and infinite Le number. Although the reaction front dynamics bear some similarity to a regular flame with finite, greater-than-unity Le number, a theory based on finite Le number is fundamentally inapplicable to describe the combustion behavior with infinite Le. Analytical results are derived to describe to evolution of reaction front velocity and temperature accounting for the effects of changing curvature as well as the ignition energy. A simplified, explicit formula is also derived to describe the reaction front propagation velocity by directly linking to the burnt temperature, exhibiting very good performance in thermal runaway propagation prediction and experimental design. The results also show smaller critical radius and minimum ignition energy for cylindrical reaction front, leading to greater concerns for thermal runaway propagation triggered by nail penetration, as compared to a local hot spot.

Keywords

Spherical reaction front, cylinder reaction front, battery thermal runaway, solid combustion, infinite Le number

Nomenclature[1]

ρ	Density
c_p	Specific heat under constant pressure
T	Temperature
t	time
U	Reaction front propagation velocity
ω	Reaction rate
Y	Mass fraction
r	Radial coordinate
R	Reaction front radius
E_a	Activation energy
R_u	Universal gas constant
λ	Thermal conductivity
ξ	Radial coordinate relative to the reaction front
ΔH	Formation enthalpy of the reactant
T_u	Unburnt temperature
T_b	Burnt temperature
Y_u	Unburnt mass fraction

---

[1] Symbols with ˜ hat denote the corresponding dimensionless quantity

s	Integration variable
α	Thermal diffusivity $\alpha = \lambda/\rho c_p$
T_{ad}	Adiabatic flame temperature
A	Pre-exponential factor of the reaction rate constant
T_{in}	Inner zone temperature variable
ε	Small perturbation parameter in the order of 1/Ze
θ	Inner zone temperature perturbation
χ	Stretched coordinate relative to the reaction front, $\chi = \xi/\varepsilon$
Ze	Zel'dovich number, $Ze = \frac{E_a}{R_u T_b^2}(T_b - T_u)$
Ze_{ad}	Ze based on adiabatic flame temperature, $Ze_{ad} = \frac{E_a}{R_u T_{ad}^2}(T_{ad} - T_u)$
U_p	Propagation speed for a planar reaction front
Le	Lewis number, α/D
δ	Characteristic reaction front thickness $\delta = \alpha/U_p$
σ	Thermal expansion ratio, T_{ad}/T_u
K	Stretch rate
D	Mass diffusivity
K_{ext}	Extinction stretch rate
Q	Ignition heat source intensity
T_f	Flame temperature

1. Introduction

As global emphasis is being put on decarbonization and carbon neutrality, battery development and application has received more and more research interest. In fact, if the electricity comes from clean energy with low pollutant emission and integrated carbon capture, a battery does have a great potential to become a centralized power storage and conversion device in the future. However, there are many other critical issues to be resolved for battery research and development [1-2], including rare earth element exploitation, battery material preparation, life-cycle enhancement, battery recycling and battery safety control, etc. Among these challenges, battery thermal runaway and runaway propagation [3-4] directly threatens properties and lives, which is fundamentally a combustion problem with reaction-transport coupling.

During thermal runaway, side reactions can occur between different battery components, for example, Solid-Electrolyte-Interphase (SEI) decomposition, cathode decomposition and cathode-electrolyte reaction, anode-electrolyte reaction, and electrolyte decomposition, which is accompanied with substantial heat release and followed by thermal runaway propagation and fires. The rates of these reaction can frequently be measured through differential scanning calorimeter (DSC) and/or Accelerating rate calorimetry (ARC) experiments. More details on the thermal runaway chemical kinetics can be found in [5-8].

In addition to complex chemical kinetics, actual thermal runaway processes can be more complicated due to the heterogeneous nature of the battery such as layered structure, porosity, solid-liquid components. However, one of the simplest yet reasonable model to describe such a phenomenon can be established by drawing analogy with solid phase combustion, where a battery is considered as a homogeneous, isotropic, solid reactive mixture. In addition, electrolyte vaporization and battery component decomposition into gas phase species are both possible during thermal runaway. In fact, venting gas emission from the battery frequently includes CH_4, C_2H_4 and other flammable small hydrocarbons, and serves as a key mechanism for battery thermal runaway propagation among battery packs and for general electrical vehicle fires. However, compared to combustion chemistry, battery thermal runaway chemistry is more challenging and is still at its infant stage. Modeling of venting gas emission is not included in the state-of-the-art thermal runaway mechanism, and is still ongoing research. For simplicity, the coupling with gas phase reactions is not included in the current study. With these assumptions, the establishment of a

thermal runaway theory is *feasible* and the reaction-conduction nature of the problem allows inherent similarity to many other combustion phenomena, such as solid propellant combustion [9], self-propagation high-temperature synthesis [10], thermal power waves [11], etc. Meanwhile, there exists clear evidence from both experimental and numerical studies suggesting a propagating-wave behavior during battery thermal runaway propagation [12-14].

Compared to gas phase combustion, reaction front initiation and propagation in solid is less studied. A naïve expectation is to directly transform the well-established gas phase flame theory based on finite Lewis number (*Le*) assumption to the solid phase scenario where mass diffusion is fundamentally absent in the time scale of interest. However, such a wishful hope is fundamentally misleading due to the singular perturbation nature of the problem as *Le* approaches infinity [15]. Actually, almost all flame theories based on finite *Le* number fail when taking the limit toward infinity *Le*. For example, the classical theory for laminar flames shows that burning flux is proportional to the square root of *Le* [16], which indicates infinite burning flux when *Le* approaches infinity. Such a difficulty is due to the fact that dropping the second-order mass diffusion term directly alters the mathematical nature of the governing equation. In fact, this is similar to the classical fluid mechanics problem with large Reynolds number, where viscous effect and the well-known Blasius equation and similarity solution is dominant in the thin boundary layer adjacent to the wall, while inviscid Euler flow dominates in the outer mean flow. Due to the different controlling physics, the inviscid flow is by no means a perturbation from the viscous solution, and vice versa.

Therefore, theory of solid combustion has to be separately developed. A pioneering work for reaction front propagation in solid materials is by Weber, Mercer and coworkers [17-18], where the propagation velocity for a quasi-steady propagation in a one-dimensional planar configuration is derived analytically using a large β asymptotic analysis. Although this method is recently extended to accommodate arbitrary ambient temperature [19], it is still limited to constant wave speed and the results cannot be mapped to the commonly used large *Ze* number asymptotic analysis. Williams [20] tackled the reaction front propagation in solid material very systematically, however, the zero-order reaction assumption utilized in the analysis removes the negative feedback from reactant consumption and hence make little difference in the inner reaction zone structure compared to a regular gas phase flame.
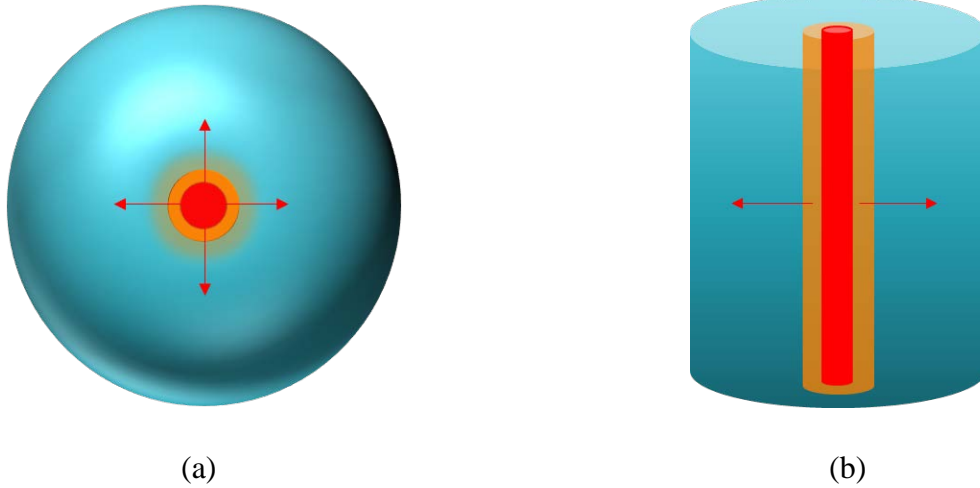
Fig. 1 Schematic of (a) spherical and (b) cylindrical reaction fronts in solid materials.

Our recent work [15] has rigorously demonstrated the fundamental differences in reduced mathematical models, controlling physical parameters, discontinuity in propagation speed, dominant balance in reaction zone structure for planar reaction front in the finite and infinite Le number conditions. In addition, we also compared the planar reaction front propagation in the largely Ze limit and the large β limit based on a different nondimensionalization and dimensionless parameter. To describe battery thermal runaway propagation and general solid combustion, the geometry and curvature of the reaction front must be sufficiently considered, which can substantially affect the propagation speed and the burnt temperature through local heat transfer and changes in energy balance. As shown in the schematic plot in Fig. 1, typical thermal runaway scenarios include those induced by a hot spot in a spherical coordinate, and those in the cylindrical geometry as triggered by nail penetration. By drawing analogy with the initiation and propagation of gaseous spherical flames [21-24] and following up with our recent work in the 1D planar coordinate [15, 19], we shall conduct theoretical asymptotic analysis for both spherical and cylindrical reaction front to evaluate the effect of curvature for curved reaction front propagation in solid materials. By further modifying the boundary condition and adding an ignition source term, a combined analysis for reaction front initiation and propagation in solid materials will be conducted.

In summary, the objective and unique contribution of the current work is to further demonstrate the effects of curvature on reaction front propagation with infinite Lewis number, and to develop a unified initiation and propagation theory accounting for both curvature and ignition

energy. Given the singular perturbation as Le approaching infinity, this is a unique problem that needs separate theoretical treatment and embodies unique physical behaviors. Our work is based on, and of equal significance to the classical gas-phase flame initiation theory, given the importance of reaction front initiation and propagation in battery and other solid materials.

2. Analysis of reaction front propagation in solids without ignition source

2-1 Theoretical analysis of spherical reaction front

Let's first consider a spherical reaction front in solid initiated from a hot spot or point source, with unsteady, diffusion and reaction processes in a laboratory coordinate. We shall first focus on propagation dynamics, and then extend the theory to incorporate initiation analysis by modifying the boundary condition. By adopting the coordinate attached to the expanding reaction front located at $\xi = r - R(t) = 0$ with a velocity $U = U(R)$ and assuming first order Arrhenius reaction $\omega = A\rho Y e^{-\frac{E_a}{R_u T}}$ and quasi-steady propagation, convection induced by relative motion is included and the unsteady term is absent:

$$-\rho c_p U \frac{dT}{d\xi} = \frac{\lambda}{(\xi+R)^2} \frac{d}{d\xi}\left[(\xi + R)^2 \frac{dT}{d\xi}\right] + \Delta H \omega \tag{1}$$

$$-\rho U \frac{dY}{d\xi} = -\omega \tag{2}$$

Subject to the boundary conditions:

$$T = T_b, Y = 0 \ at \ \xi = -R \tag{3a}$$
$$T = T_u, Y = Y_u \ at \ \xi \to +\infty \tag{3b}$$

In the outer zone solution away from the thin reaction region at $\xi = 0$, the chemical reaction is negligible due to either reactant depletion or the low temperature chemical frozen condition. By further applying the boundary condition $T(\xi = 0) = T_b$, we can have the outer solution as:

$$T = \begin{cases} T_b \ (-R \le \xi < 0) \\ T_u + \frac{T_b - T_u}{\int_R^{+\infty} s^{-2} e^{-Us/\alpha} ds} \int_{R+\xi}^{+\infty} s^{-2} e^{-Us/\alpha} ds \ (\xi > 0) \end{cases} \tag{4-a & b}$$

where the thermal diffusivity $\alpha = \lambda/\rho c_p$. Clearly the outer solution is continuous but not differentiable at $\xi = 0$, where a thin transition inner reaction zone with dominant effects from reaction and conduction should be acquired.

By combining (1) and (2) and canceling the reaction term, we can obtain:

$$\frac{\lambda}{(\xi+R)^2}\frac{d}{d\xi}\left[(\xi+R)^2\frac{dT}{d\xi}\right] + \rho c_p U \frac{dT}{d\xi} + \Delta H \rho U \frac{dY}{d\xi} = 0 \qquad (5)$$

That is:

$$\frac{d^2T}{d\xi^2} + 2\frac{d}{d\xi}\left(\frac{T}{\xi+R}\right) + \frac{2T}{(\xi+R)^2} + \frac{U}{\alpha}\frac{dT}{d\xi} + \frac{\Delta H \rho U}{\lambda}\frac{dY}{d\xi} = 0 \qquad (6)$$

Integrating once from 0 to ξ and applying the boundary conditions we can obtain the Shvab-Zel'dovich conserved scalar:

$$\frac{dT}{d\xi} - \frac{dT}{d\xi}\Big|_{\xi=0} + \left(\frac{2T}{\xi+R} - \frac{2T_b}{R}\right) + \int_0^\xi \frac{2T}{(s+R)^2}ds + \frac{U(T-T_b)}{\alpha} + \frac{\Delta H \rho U(Y-0)}{\lambda} = 0 \qquad (7)$$

Where:

$$\frac{2T_u\xi}{R(\xi+R)} = \int_0^\xi \frac{2T_u}{(s+R)^2}ds \leq \int_0^\xi \frac{2T}{(s+R)^2}ds \leq \int_0^\xi \frac{2T_b}{(s+R)^2}ds = \frac{2T_b\xi}{R(\xi+R)} \qquad (8)$$

For ξ close to zero, the upper bound is a better estimation; while for very large ξ in the far upstream, the lower bound is a better estimation. In the limit of $\xi \to +\infty$, from Eq. (7), we can have:

$$T_b - T_u = \frac{\Delta H \rho U Y_u}{\lambda\left(\frac{2}{R}+\frac{U}{\alpha}\right)} \qquad (9)$$

So a small radius with large curvature substantially reduces the reaction front temperature. As $R \to +\infty$, a spherical reaction front approaches a planar one and the effect of curvature becomes negligible and Eq. (9) degenerates to the adiabatic relationship: $T_{ad} - T_u = \frac{\Delta H Y_u}{c_p}$, where T_{ad} is the adiabatic flame temperature, and $T_b < T_{ad}$ holds for a spherical reaction front in general. For some ξ falls in the thin reaction zone, we can estimate $\int_0^\xi \frac{2T}{(s+R)^2}ds$ by using an average temperature of T and T_b, such that $\int_0^\xi \frac{2T}{(s+R)^2}ds \approx \frac{\xi(T_b+T)}{R(\xi+R)}$. Substituting back to Eq. (7), it can be reorganized as:

$$\frac{dT}{d\xi} + (T-T_b)\left(\frac{1}{\xi+R} + \frac{1}{R}\right) + \frac{U(T-T_b)}{\alpha} + \frac{\Delta H \rho U Y}{\lambda} = 0 \qquad (10)$$

Therefore, the concentration Y can be expressed as a function of T and Eq. (1) will become:

$$\frac{d^2T}{d\xi^2} + \frac{2}{\xi+R}\frac{dT}{d\xi} + \frac{U}{\alpha}\frac{dT}{d\xi} + \frac{A}{U}\left[-\frac{dT}{d\xi} - (T-T_b)\left(\frac{1}{\xi+R} + \frac{1}{R}\right) - \frac{U(T-T_b)}{\alpha}\right]e^{-\frac{E_a}{R_uT}} = 0 \qquad (11)$$

In the thin inner reaction zone, we introduce an inner temperature variable $T_{in} = T_b - \varepsilon\theta + O(\varepsilon^2)$ and a stretched coordinate $\chi = \xi/\varepsilon$, where ε is a small parameter to be determined later. Substituting back to Eq. (11), we can obtain:

$$\frac{d^2\theta}{d\chi^2} + \frac{2\varepsilon}{\varepsilon\chi+R}\frac{d\theta}{d\chi} + \varepsilon\frac{U}{\alpha}\frac{d\theta}{d\chi} + \frac{A}{U}\left[-\varepsilon\frac{d\theta}{d\chi} - \varepsilon^2\theta\left(\frac{1}{\varepsilon\chi+R} + \frac{1}{R}\right) - \varepsilon^2\frac{U\theta}{\alpha}\right]e^{-\frac{E_a}{R_u(T_b-\varepsilon\theta)}} = 0 \qquad (12)$$

Where θ satisfies the following boundary conditions:

$$\theta(\chi = 0) = 0, \frac{d\theta}{d\chi}(\chi = 0) = 0, \varepsilon\theta(\chi \to +\infty) = T_b - T_u \qquad (13)$$

Note that $\frac{1}{\varepsilon\chi+R} = \frac{1}{R(1+\varepsilon\frac{\chi}{R})} = \frac{1}{R}\left(1 - \varepsilon\frac{\chi}{R}\right)$ and that $\frac{E_a}{R_u(T_b-\varepsilon\theta)} = \frac{E_a}{R_uT_b(1-\frac{\varepsilon\theta}{T_b})} = \frac{E_a}{R_uT_b}\left(1 + \frac{\varepsilon\theta}{T_b}\right)$, Eq. 12

becomes:

$$\frac{d^2\theta}{d\chi^2} + \frac{2\varepsilon}{R}\left(1 - \varepsilon\frac{\chi}{R}\right)\frac{d\theta}{d\chi} + \varepsilon\frac{U}{\alpha}\frac{d\theta}{d\chi} + \frac{A}{U}\left[-\varepsilon\frac{d\theta}{d\chi} - \varepsilon^2\theta\left(\frac{2}{R} - \varepsilon\frac{\chi}{R^2}\right) - \varepsilon^2\frac{U\theta}{\alpha}\right]e^{-\frac{E_a}{R_uT_b}(1+\frac{\varepsilon\theta}{T_b})} = 0 \qquad (14)$$

Ignoring $O(\varepsilon)$ and $O(\varepsilon^2)$ terms, the controlling balance in the inner reaction zone is:

$$\frac{d^2\theta}{d\chi^2} - \varepsilon\frac{A}{U}\frac{d\theta}{d\chi}e^{-\frac{E_a}{R_uT_b}(1+\frac{\varepsilon\theta}{T_b})} = 0 \qquad (15)$$

Eq. (15) is identical to the inner structure relation under the planar case under Le infinity [15]. The fact that that all the terms containing curvature factor $\frac{1}{R}$ are of second or lower order and hence are completely dropped out, indicates that curvature and stretch will not affect the reaction zone structure to the leading order. Instead, the role of curvature will be reflected in the outer zone solution through the upstream preheat zone temperature profile. In other words, in the infinite Le limit, the outer solutions exhibit both qualitatively and quantitatively changes, as species diffusion term is ignored. Consequently, the difference in outer zone solution gives different constraints and matching conditions for the inner reaction zone solution. This is the challenge for a unified asymptotic analysis for arbitrary Le numbers. Eq. (15) can be integrated once with the boundary condition (13) to obtain:

$$\frac{d\theta}{d\chi}(\chi \to +\infty) = \varepsilon \frac{A}{U} e^{-\frac{E_a}{R_u T_b}} \frac{R_u T_b^2}{E_a} \left[e^{-\frac{E_a}{R_u T_b^2}(T_b - T_u)} - 1 \right] \tag{16}$$

Note that the parameter group $\frac{E_a}{R_u T_b^2}(T_b - T_u)$ is the Zel'dovich number Ze, which is a large dimensionless number. We can hence choose $\varepsilon = \frac{1}{Ze}$, such that the exponent $\varepsilon \frac{E_a}{R_u T_b^2}\theta = \frac{\theta}{T_b - T_u}$ is always O (1).

Eq. (16) must match the inner gradient of the outer solution from Eq. (4b) as $\chi \to 0$, i.e.,

$$\frac{dT}{d\chi}(\chi \to 0) = -\varepsilon \frac{T_b - T_u}{\int_R^{+\infty} s^{-2} e^{-Us/\alpha} ds} \frac{1}{R^2} e^{-UR/\alpha} \tag{17}$$

Therefore, the propagation velocity of the spherical reaction front must satisfy:

$$\frac{U R^{-2} e^{-UR/\alpha}}{\int_R^{+\infty} s^{-2} e^{-Us/\alpha} ds} = \frac{A}{Ze} e^{-\frac{E_a}{R_u T_b}}(1 - e^{-Ze}) \tag{18}$$

Given the largeness of Ze number, $e^{-Ze} \approx 0$, hence Eq. (18) can be further simplified as:

$$\frac{U R^{-2} e^{-UR/\alpha}}{\int_R^{+\infty} s^{-2} e^{-Us/\alpha} ds} = \frac{A}{Ze} e^{-\frac{E_a}{R_u T_b}} \tag{19}$$

In the limit of a planar reaction front, it can be shown that $\lim\limits_{R \to +\infty} \frac{U R^{-2} e^{-UR/\alpha}}{\int_R^{+\infty} s^{-2} e^{-Us/\alpha} ds} = \frac{U^2}{\alpha}$, also

$T_b = T_{ad}$, and hence U degenerates to the planar result $U_p = \sqrt{\frac{\alpha A}{Ze_{ad}} e^{-\frac{E_a}{R_u T_{ad}}}}$ with infinite Le

number, as shown in our previous work [15], where Ze_{ad} is the Zel'dovich number based on the adiabatic temperature, i.e., $Ze_{ad} = \frac{E_a}{R_u T_{ad}^2}(T_{ad} - T_u)$. Such consistency further justifies the current theory. The burnt temperature T_b and the propagation speed U can be determined by Eqs. (9) and (19).

The velocity, radius and temperature can be non-dimensionalized as:

$$\widetilde{U} = \frac{U}{U_p}, \widetilde{R} = \frac{R}{\delta}, \widetilde{T_b} = \frac{T_b - T_u}{T_{ad} - T_u}$$

where $\delta = \alpha/U_p$. Considering that $T_{ad} - T_u = \frac{\Delta H Y_u}{c_p}$, Eqs (9) and (19) can be transferred in the general non-dimensional form as:

$$\widetilde{T_b}\left(\widetilde{U} + \frac{2}{\tilde{R}}\right) = \widetilde{U} \tag{20}$$

$$\frac{\widetilde{U}\tilde{R}^{-2}e^{-\widetilde{U}\tilde{R}}}{\int_{\tilde{R}}^{+\infty}s^{-2}e^{-\widetilde{U}s}ds} = \frac{1}{\widetilde{T_b}}\left[\frac{\widetilde{T_b}(\sigma-1)+1}{\sigma}\right]^2 e^{Ze_{ad}\left[\frac{(\widetilde{T_b}-1)\sigma}{\widetilde{T_b}(\sigma-1)+1}\right]} \tag{21}$$

σ is the thermal expansion ratio defined as T_{ad}/T_u. It is emphasized here again that from Eq. (20), $\widetilde{T_b}$ always less than unity for a spherical reaction front, indicating sub-adiabatic condition due to the curvature effect. Now if we substitute the expression of $\widetilde{T_b}$ from Eq. (20) into Eq. (21), we can obtain an equation that only contains $\widetilde{U}$ and $\tilde{R}$, which can readily generate $\widetilde{U}$ as $\tilde{R}$ changes.

For large $\tilde{R}$, the term on of LHS of Eq. (21) can be expanded in power series of $1/\tilde{R}$ from Taylor expansion (see the supplementary material for more details):

$$\frac{\tilde{R}^{-2}e^{-\widetilde{U}\tilde{R}}}{\int_{\tilde{R}}^{+\infty}s^{-2}e^{-\widetilde{U}s}ds} = \widetilde{U} + \frac{2}{\tilde{R}} - \frac{2}{\widetilde{U}\tilde{R}^2} + O(\frac{1}{\tilde{R}^3}) \tag{22}$$

Substitute Eqs. (20) and (22) into Eq. (21), we can have:

$$\frac{\widetilde{U}^2[\widetilde{U}+\frac{2}{\tilde{R}}+O\left(\frac{1}{\tilde{R}^2}\right)]}{\left(\widetilde{U}+\frac{2}{\tilde{R}}\right)} = \left[\frac{\widetilde{T_b}(\sigma-1)+1}{\sigma}\right]^2 e^{Ze_{ad}\left[\frac{(\widetilde{T_b}-1)\sigma}{\widetilde{T_b}(\sigma-1)+1}\right]} \tag{23}$$

By ignoring the second and higher order terms, $\left(\widetilde{U} + \frac{2}{\tilde{R}}\right)$ term on the LHS of Eq. (23) can be directly canceled, indicating the same effect from curvature on the reduction of $\widetilde{U}$ and $\widetilde{T_b}$. Eq. (23) becomes:

$$\widetilde{U}^2 = \left[\frac{\widetilde{T_b}(\sigma-1)+1}{\sigma}\right]^2 e^{Ze_{ad}\left[\frac{(\widetilde{T_b}-1)\sigma}{\widetilde{T_b}(\sigma-1)+1}\right]} \tag{24}$$

which further leads to an explicit formula of $\widetilde{U}$ as a function of the burnt temperature $\widetilde{T_b}$:

$$\widetilde{U} = \frac{\widetilde{T_b}(\sigma-1)+1}{\sigma} e^{\frac{Ze_{ad}}{2}\left[\frac{(\widetilde{T_b}-1)\sigma}{\widetilde{T_b}(\sigma-1)+1}\right]} \tag{25}$$

As $\tilde{R} \to +\infty$, $\widetilde{T_b} \to 1$, and it is obvious the RHS of Eq. (25) approaches unity, which means the velocity approaches that of the planar reaction front. We can therefore justify Eq. (25) by comparing the results with those obtained from Eqs. (20) and (21).

2.2 Theoretical analysis of cylindrical reaction front

The above methodology can be easily extended to the cylindrical reaction front. Let's further consider an axisymmetric cylindrical reaction front initiate from a line source, for example, a typical scenario will be a nail penetration event that triggers battery thermal runaway. By adopting the coordinate attached to the reaction front located at $\xi = r - R(t) = 0$ with a velocity $U = U(R)$ and assume first order Arrhenius reaction $\omega = A\rho Y e^{-\frac{E_a}{R_u T}}$ and quasi-steady propagation:

$$-\rho c_p U \frac{dT}{d\xi} = \frac{\lambda}{\xi + R} \frac{d}{d\xi}\left[(\xi + R)\frac{dT}{d\xi}\right] + \Delta H \omega \tag{26}$$

$$-\rho U \frac{dY}{d\xi} = -\omega \tag{27}$$

Subject to the boundary conditions:

$$T = T_b, Y = 0 \; at \; \xi = -R \tag{28a}$$
$$T = T_u, Y = Y_u \; at \; \xi \to +\infty \tag{28b}$$

The outer solution away from the thin reaction region at $\xi = 0$ is:

$$T = \begin{cases} T_b \; (-R \le \xi < 0) \\ T_u + \frac{T_b - T_u}{\int_R^{+\infty} s^{-1} e^{-Us/\alpha} ds} \int_{R+\xi}^{+\infty} s^{-1} e^{-Us/\alpha} ds \; (\xi > 0) \end{cases} \tag{29-a \& b}$$

By defining the Shvab-Zel'dovich conserved scalar, we can again obtain the energy conservation identity similar but different to Eq. (9):

$$T_b - T_u = \frac{\Delta H \rho U Y_u}{\lambda\left(\frac{1}{R} + \frac{U}{\alpha}\right)} = \frac{(T_{ad} - T_u)U}{\frac{\alpha}{R} + U} \tag{30}$$

Similar to the spherical case, it can be shown that the inner structure equation is independent of the curvature effect, such that the inner zone equation and the outer temperature gradient of the inner solution are exactly the same as Eqs. (15) and (16). The outer temperature gradient of the inner solution must match with the inner gradient of the out solution in (29-b), as $\chi \to 0$:

$$\frac{dT}{d\chi}(\chi \to 0) = -\varepsilon \frac{T_b - T_u}{\int_R^{+\infty} s^{-1} e^{-Us/\alpha} ds} \frac{1}{R} e^{-UR/\alpha} \tag{31}$$

12

Set (31) and (16) equal:

$$\frac{UR^{-1}e^{-UR/\alpha}}{\int_R^{+\infty} s^{-1}e^{-Us/\alpha}ds} = \frac{A}{Ze} e^{-\frac{E_a}{R_u T_b}} \tag{32}$$

As R approaches infinity, we can have $\lim\limits_{R\to+\infty} \frac{UR^{-1}e^{-UR/\alpha}}{\int_R^{+\infty} s^{-1}e^{-Us/\alpha}ds} = \frac{U^2}{\alpha}$, and meanwhile $T_b =$

T_{ad}, Eq. (32) degenerates to the planar velocity, $U_p = \sqrt{\frac{\alpha A}{Ze_{ad}} e^{-\frac{E_a}{R_u T_{ad}}}}$. Using the same non-

dimensionalization as in the spherical case, Eqs. (30) and (32) become:

$$\widetilde{T_b}\left(\widetilde{U} + \frac{1}{\tilde{R}}\right) = \widetilde{U} \tag{33}$$

$$\frac{\widetilde{U}\tilde{R}^{-1}e^{-\widetilde{U}\tilde{R}}}{\int_{\tilde{R}}^{+\infty} s^{-1}e^{-\widetilde{U}s}ds} = \frac{1}{\widetilde{T_b}}\left[\frac{\widetilde{T_b}(\sigma-1)+1}{\sigma}\right]^2 e^{Ze_{ad}\left[\frac{(\widetilde{T_b}-1)\sigma}{\widetilde{T_b}(\sigma-1)+1}\right]} \tag{34}$$

(33) and (34) are inherently similar to the spherical solution (20) and (21), but subject to a reduced curvature effect. Similarly, for large $\tilde{R}$, the LHS of Eq. (34) can be expanded in power series of $1/\tilde{R}$:

$$\frac{\tilde{R}^{-1}e^{-\widetilde{U}\tilde{R}}}{\int_{\tilde{R}}^{+\infty} s^{-1}e^{-\widetilde{U}s}ds} = \widetilde{U} + \frac{1}{\tilde{R}} - \frac{1}{\widetilde{U}\tilde{R}^2} + O\left(\frac{1}{\tilde{R}^3}\right) \tag{35}$$

Therefore, similar to Eq. (23), we can have:

$$\frac{\widetilde{U}^2\left[\widetilde{U}+\frac{1}{\tilde{R}}+O\left(\frac{1}{\tilde{R}^2}\right)\right]}{\left(\widetilde{U}+\frac{1}{\tilde{R}}\right)} = \left[\frac{\widetilde{T_b}(\sigma-1)+1}{\sigma}\right]^2 e^{Ze_{ad}\left[\frac{(\widetilde{T_b}-1)\sigma}{\widetilde{T_b}(\sigma-1)+1}\right]} \tag{36}$$

Ignoring the second order terms and take the square root, Eq. (36) leads to the same simplified, explicit formula for the propagation velocity as Eq. (25). This implies that the curvature imposes similar effects on propagation velocity and burnt temperature. Eq. (25) hence can capture the leading and first order effects on reaction front propagation for both spherical and cylindrical cases, and their propagation velocity should always overlap when mapping on the $\widetilde{T_b}$ space.

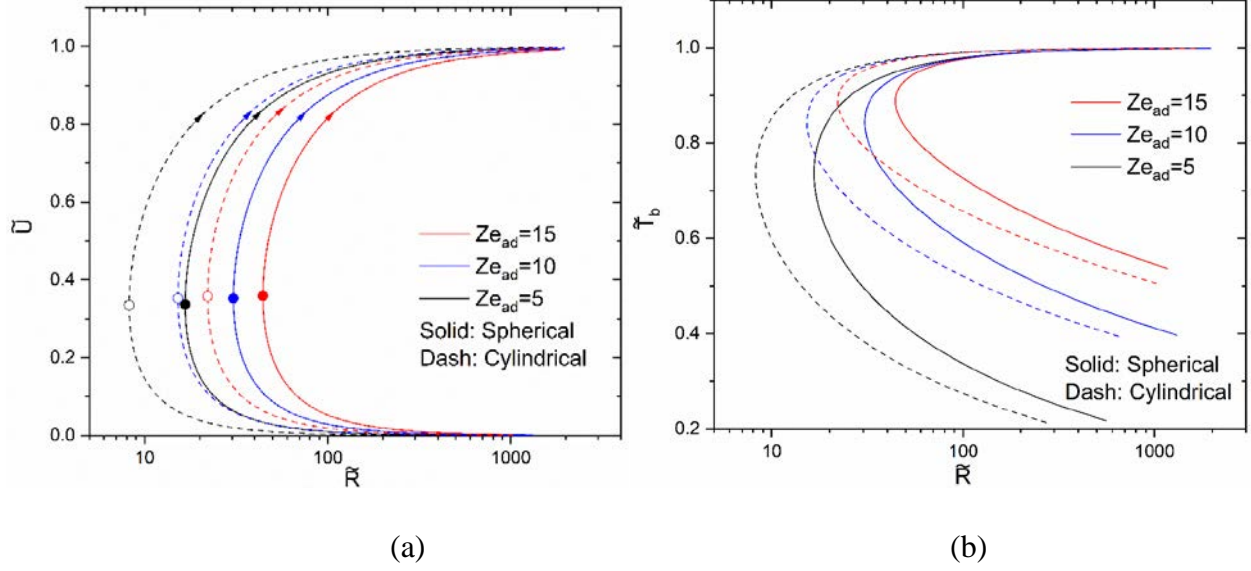2.3 Results and analysis on reaction front propagation in solids

13

<div align="center">(a)</div> <div align="center">(b)</div>

Fig. 2. Evolutions of (a) propagation velocity $\widetilde{U}$ and (b) burnt temperature $\widetilde{T_b}$ with radius $\tilde{R}$ as described by Eqs. (20) and (21) at different $Ze_{ad} = 5, 10, 15, \sigma = 7$. Arrows indicate the direction of reaction front evolution and symbols indicate the critical states.

Fig. 2 shows the evolution of $\widetilde{U}$ and $\widetilde{T_b}$ with radius at different adiabatic Zel'dovich numbers Ze_{ad} for both the spherical and cylindrical case, which both exhibit a C-shape curve response, qualitatively similar to the behavior of gaseous spherical flame with *Le* >1 [21-22]. The turning point of each C-shape curve corresponds to the critical radius and critical temperature, only beyond which can a self-sustained reaction front survive. Any reaction front with radius or temperature below the critical value will be quenched by the increased curvature effect. The upper branch of the C-shape curve contains all the achievable states, where both the propagation speed and burnt temperature drastically increases as the reaction front expands. Such increasing rate gradually decreases with increasing radius, and eventually both $\widetilde{U}$ and $\widetilde{T_b}$ approach unity for sufficiently large $\tilde{R}$~1000.
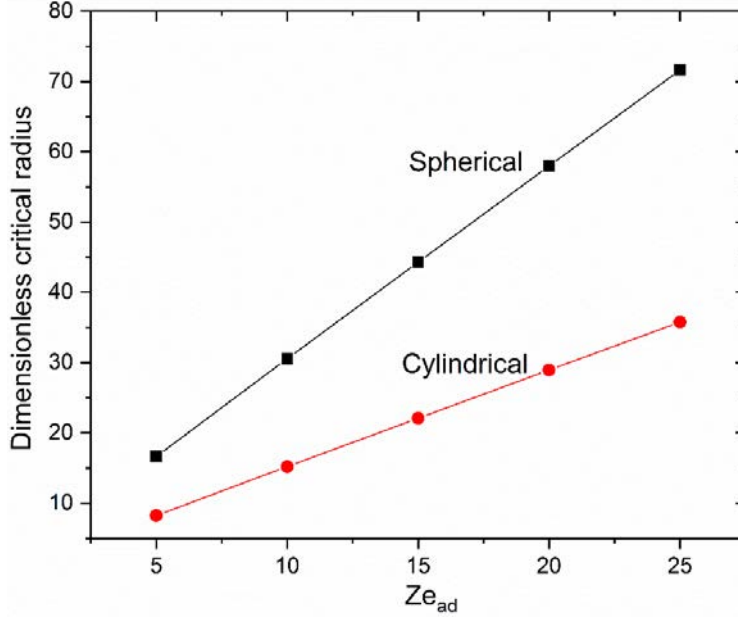
<div align="center">14</div>

Fig 3. Critical radius as a function of Ze_{ad} for both the spherical and cylindrical case.

Fig. 3 shows the dimensionless critical radius identified at the turning point of C-shape curve as a quasi-linear function of Ze_{ad}. With reduced Ze_{ad}, we can observe smaller critical radius at the turning point, which indicates that the reaction front can be triggered more easily. Furthermore, the comparison of the spherical and cylindrical cases shows that critical radius for the cylindrical configuration is exactly 50% of the value for the spherical case under the same reaction conditions, indicating that reaction front can be triggered more easily in the cylindrical case. The smaller critical radius in the cylindrical configuration can have interesting implications for battery thermal runaway, in that a nail penetration-induced thermal runaway event is potentially more dangerous compared to the event triggered by a local point source.

A classical way to show the curvature effect on reaction front dynamics is through the introduction of stretch rate. Here a dimensionless stretch rate $\widetilde{K}$ can be defined as $\widetilde{K} = \frac{1}{\tilde{A}}\frac{d\tilde{A}}{dt}$, where the dimensionless surface area is $\tilde{A} = 4\pi\tilde{R}^2$ for a sphere and $2\pi\tilde{R}h$ for a cylindrical surface with height h. Therefore, $\widetilde{K} = \frac{2}{\tilde{R}}\frac{d\tilde{R}}{dt} = \frac{2\widetilde{U}}{\tilde{R}}$ for a spherical reaction front, and $\frac{\widetilde{U}}{\tilde{R}}$ for a cylindrical reaction front. As shown in Fig. 4, there exhibit a critical stretch rate beyond which a reaction front cannot survive, and this can be defined as the extinction stretch rate, $\widetilde{K}_{ext}$, which provides the threshold residence time for the reaction front. In the upper branch above the turning point, all cases show

negative dependence on stretch rate as the reaction front expands. Strong nonlinear effects in the slope are observed in the beginning, which gradually evolve into a quasi-linear dependence as approaching to the unstretched planar reaction front at $\widetilde{K} = 0$. Similar to the gaseous spherical flame, this feature can be utilized to determine the unstretched reaction front propagation speed and Markstein length [25] in the solid materials. With decreasing Ze_{ad}, the slope becomes flatter and flatter as $\widetilde{K}$ approaches 0, showing a smaller magnitude of the Markstein length. Another important observation is that although the spherical and cylindrical reaction fronts tend to have different propagation velocities and temperatures at the same radius (shown in Fig. 2), they almost completely overlap with each other in the $\widetilde{U}$ - $\widetilde{K}$ phase plot in Fig. 4.
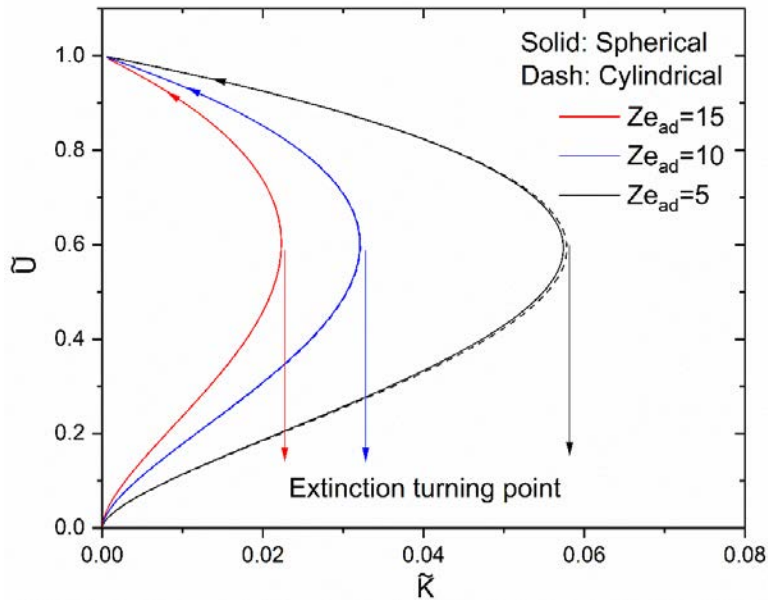

Fig. 4. Evolutions of propagation velocity $\widetilde{U}$ with dimensionless stretch rate $\widetilde{K}$ at different $Ze_{ad} = 5, 10, 15, \sigma = 7$, showing the extinction state. Arrows indicate the direction of expanding radius.

Extensive numerical and theoretical analysis have been performed for a regular gaseous spherical flame with arbitrary *Le*. It is well-known that the flame temperature, the propagation speed and the extinction stretch rate all depends on the *Le* of the mixture. Due to the absence of mass diffusion in a solid material, it is of interest to show if the combustion characteristics are consistent between a solid with infinite *Le* and a gas with asymptotically increased *Le*. Based on

the spherical flame theory [22, 24], it has been shown that the dimensionless propagation velocity and flame temperature for a finite *Le* spherical flame is (same notation in the current work):

$$\frac{\widetilde{T_b}\tilde{R}^{-2}e^{-\tilde{U}\tilde{R}}}{\int_{\tilde{R}}^{+\infty}s^{-2}e^{-\tilde{U}s}ds} = \frac{1}{Le}\frac{\tilde{R}^{-2}e^{-\tilde{U}Le\tilde{R}}}{\int_{\tilde{R}}^{+\infty}s^{-2}e^{-\tilde{U}Les}ds} = \left[\frac{\widetilde{T_b}(\sigma-1)+1}{\sigma}\right]^2 e^{\frac{Ze_{ad}}{2}\left[\frac{(\widetilde{T_b}-1)\sigma}{\widetilde{T_b}(\sigma-1)+1}\right]} \tag{37}$$

And with the following dimensional form [24]:

$$T_b = T_u + \frac{qY_u}{c_p}\frac{1}{Le}e^{\frac{UR}{\alpha}(1-Le)}\frac{\int_R^{+\infty}s^{-2}e^{-Us/\alpha}ds}{\int_R^{+\infty}s^{-2}e^{-Us/D}ds} \tag{38}$$

$$\frac{R^{-2}e^{-UR/\alpha}}{\int_R^{+\infty}s^{-2}e^{-Us/\alpha}ds} = \sqrt{\frac{2A}{Ze^2 D}}e^{-\frac{E_a}{R_u T_b}} \tag{39}$$

Where D is the mass diffusivity. Compared to the current work, there is no explicit assumption on the order of magnitude of Lewis number in the regular gas phase flame theory in the derivation of Eq. (37-39), where *Le* is an arbitrary finite number. Hence, the different behavior for finite and infinite *Le* will be solely attributed to the *Le* itself. Obviously, these results in Eqs. (37-39) lose physical meaning by taking the limit of *Le* approaching infinity. For example, in the limit of $R \to +\infty$, by further taking the limit of $Le \to +\infty$, Eq. (38) becomes $T_b = T_u$ and Eq. (39) becomes $U = \sqrt{\frac{2\alpha LeA}{Ze_{ad}^2}}e^{-\frac{E_a}{R_u T_{ad}}} \to +\infty$.

In Fig. 5, the evolution of gas phase spherical flame with various *Le* is calculated using Eq. (35), and compared with the current theory with an infinite *Le* in the $\tilde{U}$ - $\tilde{K}$ diagram. Clearly, as *Le* increases from 2 to 100, extinction occurs at lower extinction stretch rate $\tilde{K}_{ext}$, and meanwhile the magnitude of the Markstein length increases. However, the limit with infinite *Le* cannot be achieved by further increasing the *Le* using Eq. (35), instead, the case with infinite *Le* has a similar behavior as the case with *Le* = 10. In fact, to the best of the authors' knowledge, the largest Lewis number involved in gas phase fuel mixture experiment in the literature is about 5.40, which is from stoichiometric iso-octane with 21% O_2 diluted with balanced Helium [26]. The larger molecular weight of the fuel leads to smaller diffusivity, and the He dilution substantially increases the thermal diffusivity of the mixture. With large *Le*, the flame is subject to strong pulsating behavior. In the meantime, a large *Le* flame is usually subadiabatic in common flame configurations with

17

positive stretch, such as spherical bomb and counterflow, which strongly narrows the flammability limits of the mixture and leads to great challenges in the experiment.
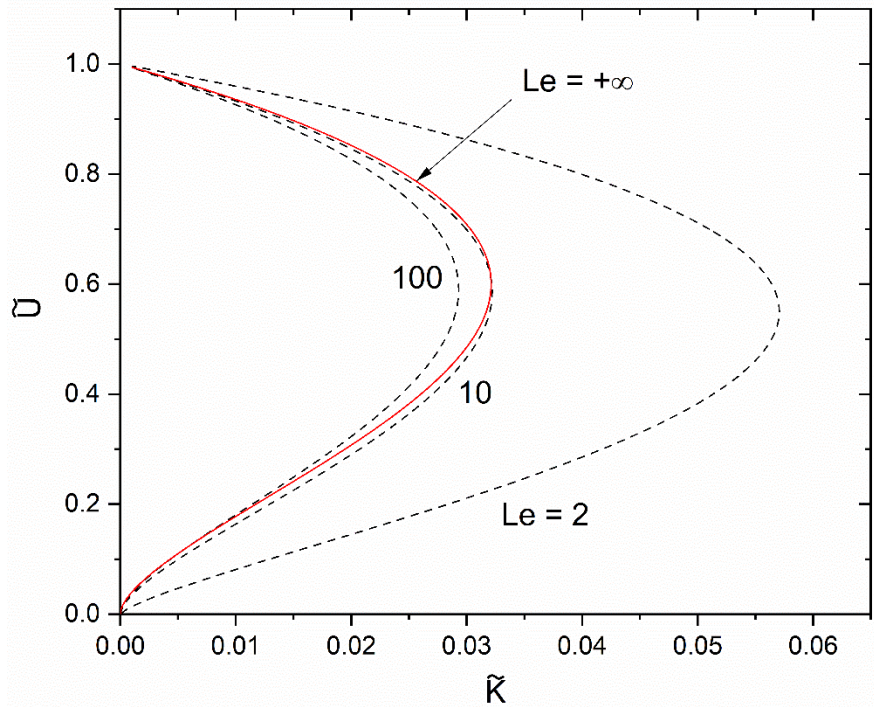

Fig. 5 Evolution of propagation velocity $\widetilde{U}$ with dimensionless stretch rate $\widetilde{K}$ at different *Le* numbers, $Ze_{ad} = 10$, $\sigma = 6.67$.

The extinction stretch rate is evaluated and shown as a function of $1/Le$ in Fig. 6, with $Ze_{ad} = 5$, $\sigma = 6.67$. It is seen that as *Le* increases, $\widetilde{K}_{ext}$ monotonically decreases, showing reduced resistance to stretch. The 10% discrepancy in the predicted value of the nondimensional extinction stretch rate does seem to quantitively support the usefulness of gas phase spherical flame theory. However, the key point in Fig. 6 is to demonstrate the mathematical discontinuity in $\widetilde{K}_{ext}$ from these two theories as *Le* approaches infinity, and hence a limit does not exist. Due to the qualitative difference of the two theories in terms of controlling parameter, reduced physical model and reaction zone structure [15], the small discrepancy in extinction stretch rate is most likely a coincidence. For other applications such as the propagation speed, the difference between the two theories can be substantial, one leads to finite prediction and the other gives infinity. Therefore, although the evolution of $\widetilde{U}$ and $\widetilde{T_b}$ and the existence of $\widetilde{K}_{ext}$ in the solid spherical reaction front bear qualitative similarities to the gaseous phase scenario with a finite *Le* greater than unity, it is

always misleading to directly take the limit of infinite *Le* to describe solid combustion based on gas phase combustion.
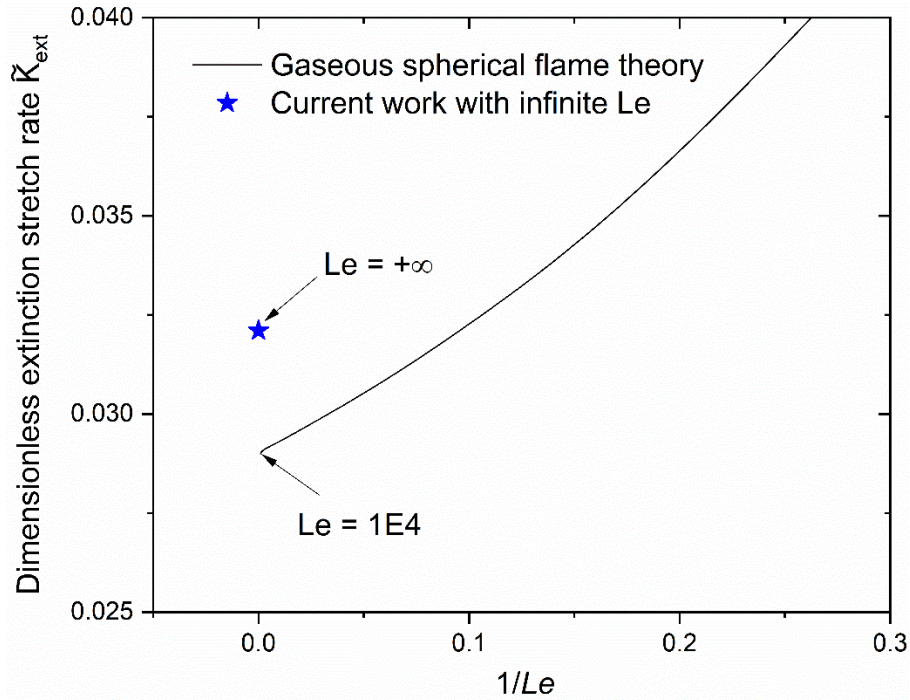

Fig. 6. Dimensionless extinction stretch rate $\widetilde{K}$ as a function of $1/Le$, showing discontinuity at infinite Le, $Ze_{ad} = 5$, $\sigma = 6.67$. The gaseous spherical flame theory is described in [24].

Lastly, we want to further justify the simple, explicit formula Eq. (25) for spherical and cylindrical reaction front propagation in solid materials. As shown in Fig. 7, the relationship between $\widetilde{U}$ and $\widetilde{T_b}$ is satisfactorily captured. The implication of Eq. (25) is highly useful, in that the propagation velocity of a spherical or cylindrical reaction front in a solid material can be uniquely and straightforwardly determined from the burnt temperature. Considering that temperature measurement is much easier for solids, it is straightforward to design experiments to measure combustion wave propagation in solids utilizing temperature measurement. It should be noted that Eq. (25) in general does not hold for gas phase combustion, where stronger coupling exists between nonequidiffusivities and curvature effects. We can easily validate the performance of Eq. (25) for cylindrical reaction front propagation in the similar way.
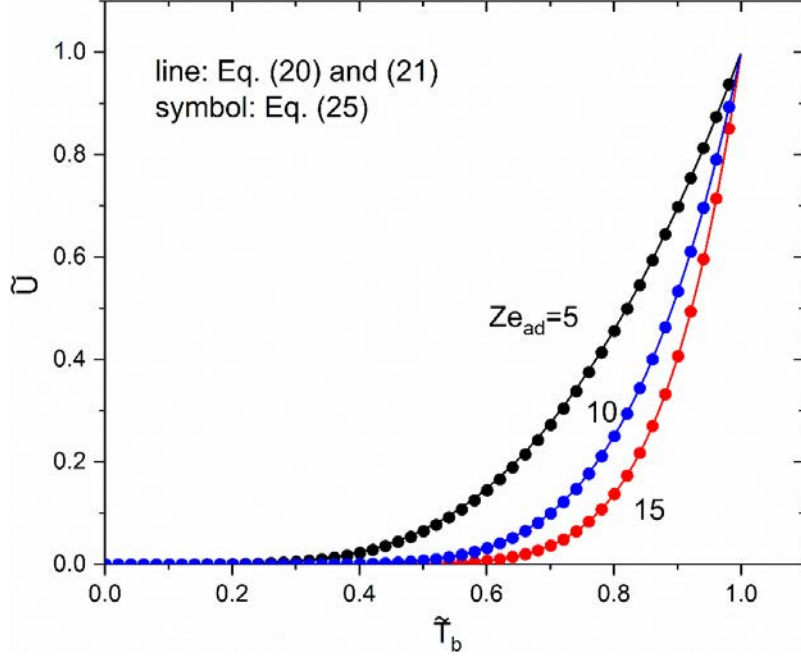
Fig. 7. Normalized propagation velocity $\widetilde{U}$ as a function of the burnt temperature $\widetilde{T_b}$, showing good performance of the simplified formula Eq. (25).

3. Further consideration of reaction front initiation with ignition source

3.1 Theoretical analysis on reaction front initiation in solids

So far Sec. 2 considers the quasi-steady propagation regime of curved reaction front in solids, without the ignition effect and hence the reaction front initiation process. In this part, we further consider a reaction front initiation in solid, by adopting the same coordinate, chemical reaction model, but with a constant ignition source Q through the boundary condition, with a dimension of Temperature x Length. In the spherical coordinate, the governing equations are the same as (1) and (2), but subject to the modified boundary conditions:

$$(\xi + R)^2 \frac{\partial T}{\partial \xi} = -Q, Y = 0 \; at \; \xi = -R \qquad (40a)$$

$$T = T_f, Y = 0 \; at \; \xi = 0 \qquad (40b)$$

$$T = T_u, Y = Y_u \; at \; \xi \to +\infty \qquad (40c)$$

T_f is now the flame temperature, which is different from the burnt temperature T_b without the ignition source. It can be shown that a particular solution of Eqs. (1) and (2) satisfying this inhomogeneous boundary condition of Eq. (40a) will be:

20

$$T' = Q \int_{R+\xi}^{+\infty} s^{-2} e^{-Us/\alpha} ds \quad (-R \le \xi < 0) \tag{41}$$

Therefore, by superimposing the general solution with homogeneous boundary condition Eq. 4 (a & b) and the particular solution with non-homogeneous boundary condition Eq (41), we can have the outer solution incorporating the effect of ignition energy:

$$T = \begin{cases} T_b + Q \int_{R+\xi}^{+\infty} s^{-2} e^{-Us/\alpha} ds \quad (-R \le \xi < 0) \\ T_u + \frac{T_f - T_u}{\int_R^{+\infty} s^{-2} e^{-Us/\alpha} ds} \int_{R+\xi}^{+\infty} s^{-2} e^{-Us/\alpha} ds \quad (\xi > 0) \end{cases} \tag{42}$$

At the immediate burnt zone of the flame front $\xi = 0^-$, $T = T_f = T_b + Q \int_R^{+\infty} s^{-2} e^{-Us/\alpha} ds$. The identity from the energy conservation equivalent to Eq. (9) can be derived as:

$$(T_f - T_u)\left(\frac{2}{R} + \frac{U}{\alpha}\right) = QR^{-2} e^{-\frac{UR}{\alpha}} + \frac{\Delta H \rho U Y_u}{\lambda} \tag{43}$$

For $Q = 0$, it is clear that $T_f = T_b$ and Eq. (43) degenerates to Eq. (9). As R approaches infinity, Eq. (43) degenerates to $T_{ad} - T_u = \frac{\Delta H Y_u}{c_p}$, showing that the adiabatic flame temperature for the planar reaction front is not being affected by the ignition energy Q. In the thin inner reaction zone, we introduce an inner temperature variable $T_{in} = T_f - \varepsilon\theta + O(\varepsilon^2)$ and the same stretch coordinate variable, we can show that all the inner zone derivation is fundamental the same as has been described in Sec. 2.1, except that all the T_b are replaced by T_f. Through matching procedure, similar to Eq. (19), we can readily show that:

$$\frac{UR^{-2} e^{-UR/\alpha}}{\int_R^{+\infty} s^{-2} e^{-Us/\alpha} ds} = \frac{A}{Ze} e^{-\frac{E_a}{R_u T_f}} \tag{44}$$

By introducing the same nondimensionalization for $\tilde{U}$ and $\tilde{R}$, as well as $\tilde{T}_f = \frac{T_f - T_u}{T_{ad} - T_u}$ and $\tilde{Q} = Q/(\frac{\Delta H Y_u \delta}{c_p})$, Eq. (43) and (44) will become:

$$\tilde{T}_f\left(\tilde{U} + \frac{2}{\tilde{R}}\right) = \tilde{Q}\tilde{R}^{-2} e^{-\tilde{U}\tilde{R}} + \tilde{U} \tag{45}$$

$$\frac{\tilde{U}\tilde{R}^{-2} e^{-\tilde{U}\tilde{R}}}{\int_{\tilde{R}}^{+\infty} s^{-2} e^{-\tilde{U}s} ds} = \frac{1}{\tilde{T}_f}\left[\frac{\tilde{T}_f(\sigma-1)+1}{\sigma}\right]^2 e^{Ze_{ad}\left[\frac{(\tilde{T}_f-1)\sigma}{\tilde{T}_f(\sigma-1)+1}\right]} \tag{46}$$

21

Eq. (45) and (46) include effects from the ignition source and hence can describe the entire reaction front initiation and propagation process in the spherical coordinate.

Following a similar procedure, we can derive the following Eq. (47) and (48) for cylindrical reaction front initiation and propagation:

$$\widetilde{T}_f\left(\widetilde{U} + \frac{1}{\tilde{R}}\right) = \tilde{Q}\tilde{R}^{-1}e^{-\tilde{U}\tilde{R}} + \widetilde{U} \tag{47}$$

$$\frac{\tilde{U}\tilde{R}^{-1}e^{-\tilde{U}\tilde{R}}}{\int_{\tilde{R}}^{+\infty} s^{-1}e^{-\tilde{U}s}ds} = \frac{1}{\widetilde{T}_f}\left[\frac{\widetilde{T}_f(\sigma-1)+1}{\sigma}\right]^2 e^{Ze_{ad}\left[\frac{(\widetilde{T}_f-1)\sigma}{\widetilde{T}_f(\sigma-1)+1}\right]} \tag{48}$$

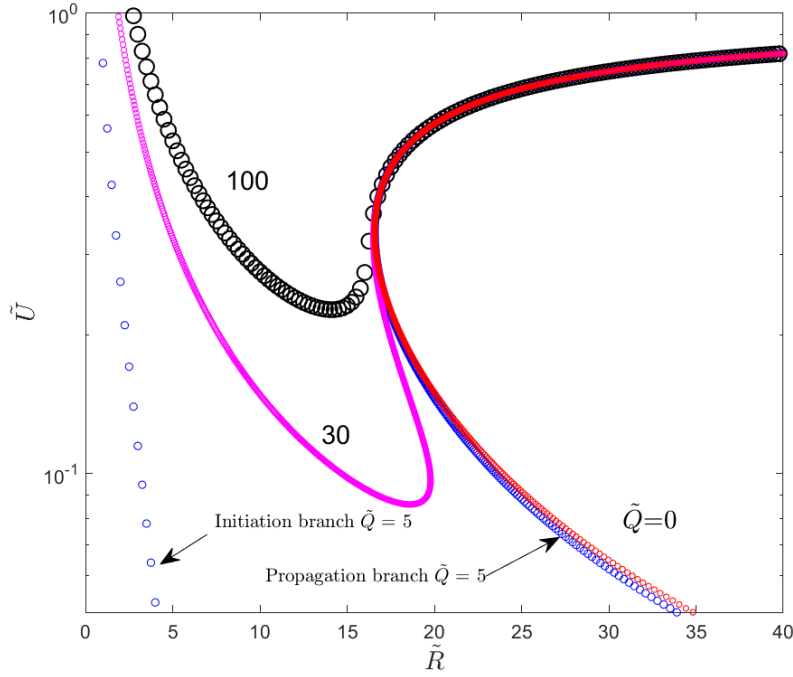3.2 Results combining reaction front initiation and propagation branches

Fig. 8. Spherical reaction front propagation velocity as a function of radius with different dimensionless ignition energy $\tilde{Q} = 0, 5, 30, 100$ based on Eqs. (45) and (46). $Ze_{ad} = 5$, $\sigma = 6.67$.

Fig. 8 shows the evolution of spherical reaction front velocity as a function of radius with different ignition energy, following the above theoretical results Eq. (45) and (46). When $\tilde{Q} = 0$, the solution only includes the C-shape propagation branch as shown in Fig. 2 with a critical radius of 15, below which no solution exists. When $\tilde{Q}$ is increased to 5, there exist two branches of solutions, including an initiation branch on the left, with decreased velocity as the kernel develops and extinguishes, as well as a propagation branch on the right, adjacent to the solution with $\tilde{Q} = 0$.

22

These two branches are separated and hence describe a failed initiation process. With further increased ignition energy $\tilde{Q} = 30$, the left initiation branch and the right propagation branch merge with each other, such that the kernel can be successfully initiated and propagate. For this case, it can be seen that close to the merging regime, the system exhibits hysteresis in the form of an S-curve, with an ignition and extinction turning point. Similar behavior is described in the spherical flame initiation as demonstrated in [21-22]. With further increased ignition energy, for example, $\tilde{Q} = 100$, such hysteresis disappears, and the folded S-curve degenerates to a stretched one. It can be seen that the two successful initiations with sufficient ignition energy both have their propagation branches eventually overlapping with the baseline case of $\tilde{Q} = 0$, demonstrating the insignificance of ignition energy from the center once a reaction front is successfully triggered. Hence, all these branches share the same critical radius around 15. The minimum ignition energy is found to be around $\tilde{Q} = 25$, which is much higher compared to the minimum ignition energy $\tilde{Q} = 0.97$ for a spherical flame with $Le = 2$ [22].
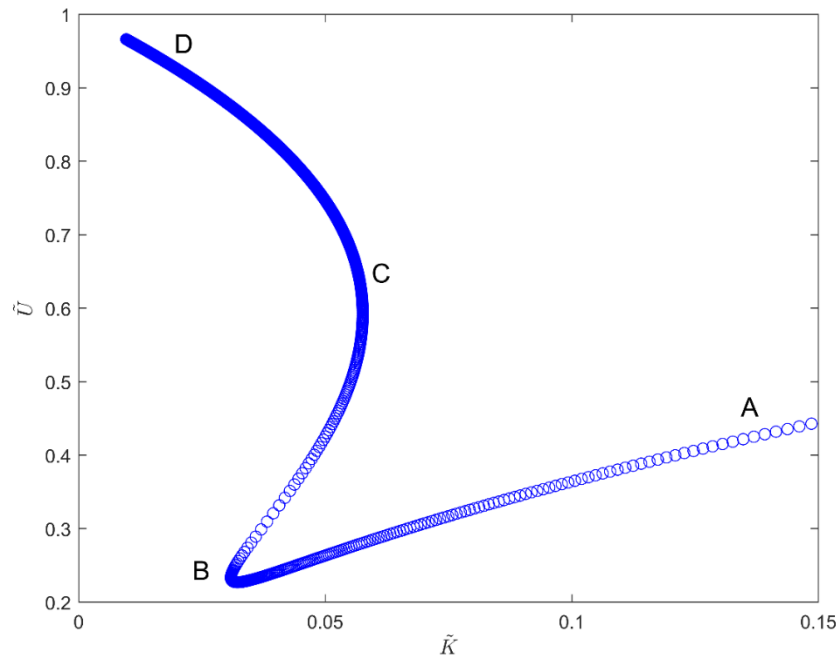

Fig. 9. Regimes of reaction front initiation and propagation, $Ze_{ad} = 5$, $\sigma = 6.67$, $\tilde{Q} = 100$.

Similar to gas phase combustion [27], the entire process of curved reaction front initiation and propagation in solid include multiple regimes, which can be readily shown on the stretch rate space. As shown in Fig 9., the evolution dimensionless propagation velocity $\tilde{U}$ is shown with

variation of the dimensionless stretch rate $\widetilde{K}$. In general, there are three distinct reaction front regimes: (I) the ignition energy induced kernel development (AB), (II) ignition kernel transition (BC), (III) the normal flame propagation (CD). Regime I (AB) is the initiation regime driven by the ignition energy Q. At the end of Regime I, the ignition kernel reaches the minimum velocity and is readily to go beyond the critical radius. In Regime II (BC), the effect from ignition energy becomes negligible, and the ignition kernel quickly expands with the driving force of chemical reaction and heat conduction. In Regime III (CD), the reaction front is mature enough and propagates quasi-steadily as it expands. The change of curvature becomes the dominant factor that controls its dynamics, before it eventually approaches the planar limit. It is worth noting that the physical regimes of reaction front initiation in gas phase mixture have been correctly identified even under the quasi-steady propagation assumption as in the theoretical work in [21] [22] based on large activation energy asymptotic analysis. More recently, the quasi-steady propagation assumption is further evaluated by [28], where analytical results of transient initiation of a premixed flame is obtained without ignoring the unsteady term. The results further justify that the quasi-steady assumption is a very good approximation in reaction front initiation analysis.
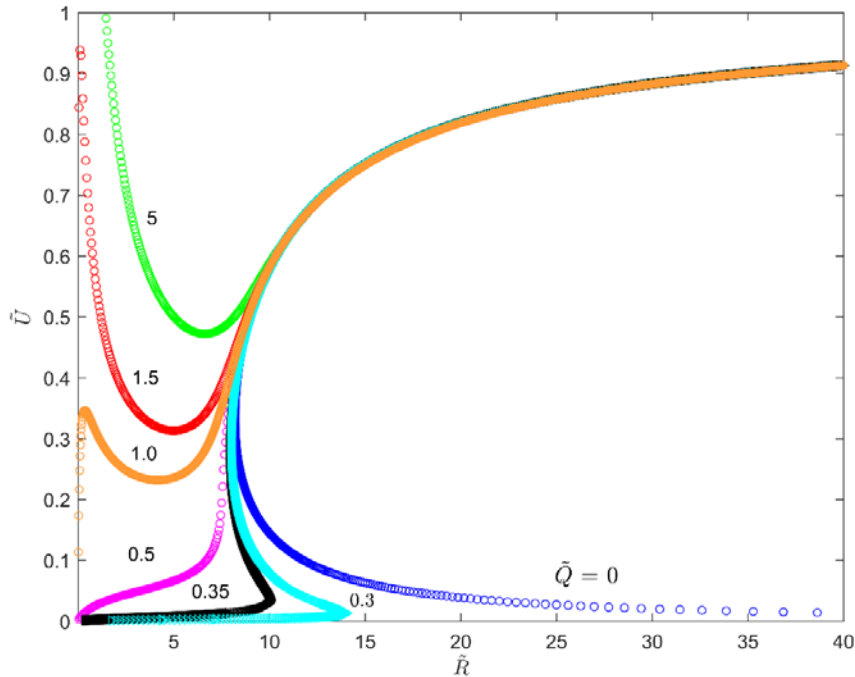

Fig. 10. Cylindrical reaction front propagation velocity as a function of radius with different dimensionless ignition energy $\widetilde{Q} = 0 \sim 5$, based on Eqs. (47) and (48). $Ze_{ad} = 5$, $\sigma = 6.67$.

Fig. 10 shows the initiation and propagation regime of the cylindrical reaction front with different ignition source, acquired based on the theoretical results in Eq. (47) and (48). When $\tilde{Q} = 0$, the solution only exhibits a C-shape propagation branch as shown above in Fig. 2. With slightly increased $\tilde{Q} = 0.3$, the initiation branch is manifested in the form a S-curve behavior with both ignition and extinction turning point, and the upper S-curve merges with the propagation branch of the solution. With continued increment in ignition energy to $\tilde{Q} = 0.5$, the folded S-curve becomes stretched, leading to monotonic and continuous kernel growth from the center. It should be noted that for the solutions around $\tilde{Q} = 0.5$ or below, given the large $\tilde{R}$ and the small $\tilde{U}$ in the lower branch of the S-curve, we can immediately realize that the system takes a very long time to actually reach the ignition state and transition to the propagation branch, and hence this kind of solution is most likely induced by the artifact of constant ignition source in the boundary with infinitely long duration time, and hence of less interest. With further increased ignition energy to $\tilde{Q} = 1.5$, the system has a similar behavior of direct initiation as the spherical case with large ignition energy, showing a local minimum in propagation velocity before bridging with the propagation branch. The minimum ignition energy in the cylindrical case that allows this kind of behavior is around $\tilde{Q} = 1$, which is much lower compared to the spherical cases, demonstrating that thermal runaway in the cylindrical geometry is more easily to occur.

Direct comparisons have been conducted with numerical simulation performed using CONVERGE and detailed runaway chemistry from [29], achieving qualitative agreement and further demonstrating the usefulness of our theory. Specifically, for the same ignition energy and same kernel size of 2 mm, the cylindrical case successfully initiates a reaction front while the spherical case fails to, due to stronger curvature effect. This is consistent with our finding that thermal runaway propagation is more likely triggered by nail penetration comparing to local hot spots. In addition, in the cylindrical case, with further reduced kernel size from 2 mm to 1.5 and 1 mm, thermal runaway fails to be initiated in both cases. This is consistent to our findings of the critical radius in thermal runaway propagation. On the other hand, the simulation with detailed chemistry has shown some pulsating behavior, consistent to the large Lewis number gas flame with pulsating instability and seminal work by Matkowsky and Sivashinsky [30] and Weber et al. [17] on solid combustion. A thermal runaway theory incorporating both curvature and pulsating merits further exploration.

Conclusion

In this work, large Ze number asymptotic analysis is performed based on infinite *Le* number and one-step global chemistry to describe the curved reaction front propagation in solid materials, with potential applications for battery thermal runaway propagation and solid combustion. The results show that although there are some qualitative similarities between the infinite *Le* number scenario with a finite, greater-than-unity *Le* case, including propagation dynamics, the existence of critical radius, dependence on stretch, etc, existing theory based on finite *Le* number cannot be directly applied to describe solid combustion where mass diffusion is completely ignored. Discontinuity in reaction front dynamics and extinction stretch rate is shown in the limit of an infinite *Le*.

The large Ze number asymptotic analysis has shown that the curvature related terms are of higher orders and hence will not affect the inner reaction zone structure. The effect of curvature is manifested through the outer zone temperature profile when matching with the inner zone gradient. Analytical formulas are derived to describe the temperature and propagation velocity during reaction front initiation and propagation, accommodating the curvature and ignition energy effects. The results also show that the cylindrical reaction front always has a smaller critical radius, 50% for the value of the spherical case, indicating greater concerns for thermal runaway propagation in the nail penetration scenario, as compared with a local hot spot. Such concern is further justified by the much lower minimum ignition energy in the cylindrical case.

It is shown that the spherical and cylindrical reaction front largely overlaps in the phase plot $\widetilde{U}$ - $\widetilde{K}$. Through perturbation analysis, the effects from curvature on the propagation velocity and temperature can be canceled out when second and higher order terms are ignored in both spherical and cylindrical case. A simple, explicit formula Eq. (25) has been developed to directly link the propagation velocity with the burnt temperature in solid combustion, which can be useful to guide experiments and estimate reaction front propagation in solids.

2D and 3D CONVERGE simulations using detailed thermal runaway chemistry have further confirmed some of the findings from the theory, such as the existence of critical radius for thermal runaway propagation and greater safety concern in the cylindrical coordinate. In the future, we shall further extend the theory to predict pulsation behaviors of the reaction front and accommodate porosity and heterogeneous nature of the materials.

Acknowledgment

Reference

[1] J. M. Tarascon, Key challenges in future Li-battery research, Philos. T. Roy. Soc. A. 368 (2010) 3227–3241.

[2] Q. Wang, B. Mao, S. I. Stoliarov, J. Sun, A review of Lithium ion battery failure mechanisms and fire prevention strategies, Prog. Energ. Combust. 73 (2019) 95-131.

[3] A. Borger, J. Mertens, H. Wenzl, Thermal runaway and thermal runaway propagation in batteries: What do we talk about? J. Energy Storage 24 (2019) 100649.

[4] L. Zhang, P. Zhao, M. Xu, X. Wang, Computational identification of the safety regime of Li-ion battery thermal runaway, Appl. Energ. 261 (2020) 114440.

[5] T.D. Hatchard, D.D. MacNeil, A. Basu, J.R. Dahn, Thermal model of cylindrical and prismatic lithium-ion cells. Journal of the Electrochemical Society 148 (2001) A755-A761.

[6] R. Spotnitz, J. Franklin, Abuse behavior of high-power, lithium-ion cells, J. Power Sources 113 (2003) 81-100.

[7] G. Kim, A. Pesaran, R. Spotnitz, A three-dimensional thermal abuse model for lithium-ion cells, Journal of Power Sources 170 (2007) 476-489.

[8] A. Garcia, J. Monsalve-Serrano, R. Sari, A. Robles, Numerical analysis of kinetic mechanisms for battery thermal runaway prediction in Li-ion batteries, Int. J. Engine Res., https://doi.org/10.1177/14680874211029902, 2021

[9] M. W. Beckstead, K. Puduppakkam, P. Thakre, V. Yang, Modeling of combustion and ignition of solid propellant ingredients, Prog. Energ. Combust. 33 (2007) 497-551.

[10] A. Makino, C. K. Law, Pulsating instability in the nonadiabatic heterogeneous SHS flame: Theory and experimental comparisons, Symp. (Int.) Combust. 26 (1996) 1867-1874.

[11] W. Choi, S. Hong, J. Abrahamson, J. Han, C. Song, N. Nair, S. Baik, M.S. Strano, Chemically driven carbon-nanotube-guided thermopower waves, Nat. Mater. 9 (2010) 423–429.

[12] J. Lamb, C. J. Orendorff, L. Steele, S. Spangler, Failure propagation in multi-cell lithium ion batteries, Journal of Power Sources 283 (2015) 517-523.

[13] A. Kurzawski, L. Torres-Castro, R. Shurtz, J. Lamb, J. Hewson, Predicting cell-to-cell failure propagation and limits of propagation in lithium-ion cell stacks, Proc. Combust. Inst. 38 (2021) 4737-4745

[14] H. Wang, Z. Du, L. Liu, Z. Zhang, J. Hao, Q. Wang, S. Wang, Study on the thermal runaway and its propagation of Li-ion batteries under low pressure, Fire Technology 56 (2020) 2427-2440.

[15] P. Zhao, Singular perturbation analysis of reaction front with infinite Lewis number: reduced model, propagation speed and reaction zone structure, Int. J. Heat Mass Tran., under review.

[16] C.K. Law, Combustion Physics, Cambridge University Press, 2006.

[17] R. O. Weber, G. N. Mercer, H. S. Sidhu, B. F. Gray, Combustion waves for gases and solids, P. Roy. Soc. Lond. A. Mat. 453 (1997) 1105–1118.

[18] A.C. Mcintosh, R. O. Weber, G. N. Mercer, Non-adiabatic combustion waves for general Lewis numbers: wave speed and extinction conditions, ANZIAM J. 46 (2004) 1-16.

[19] P. Zhao, L. Liu, Y. Chen, H. Ge, Theoretical and numerical analysis for thermal runaway propagation within a single cell, Int. J. Heat Mass Tran. 181 (2021) 121901.

[20] F.A. Williams, Combustion Theory (2nd edn), Benjamin-Cummins, Menlo Park, California USA,1985.

[21] L. He, Critical conditions for spherical flame initiation in mixtures with high Lewis numbers, Combust. Theor. Model. 4 (2000) 159-172.

[22] Z. Chen, Y. Ju. Theoretical analysis of the evolution from ignition kernel to flame ball and planar flame, Combust. Theor. Model. 11 (2007) 427-453.

[23] Z. Chen, M. P. Burke, Y. Ju, On the critical radius and minimum ignition energy for spherical flame initiation, Proc. Combust. Inst. 33 (2011) 1219-1226.

[24] Y. Wu, Z. Chen, Asymptotic analysis of outwardly propagating spherical flames, Acta Mech. Sin. 28 (2012) 359-366.

[25] P. Clavin, Dynamic behavior of premixed flame fronts in laminar and turbulent flows, Prog. Energ. Combust. 11 (1985) 1–59.

[26] *Y. Ma (2009). High-Lewis number premixed flame instabilities (Doctoral dissertation, Drexel University)*. Retrieved from URL: http://hdl.handle.net/1860/3127

[27] Y. Wang, W. Han, Z. Chen, Effects of fuel stratification on ignition kernel development and minimum ignition energy of n-decane/air mixtures, Proc. Combust. Inst. 37 (2019) 1623-1630.

[28] D. Yu, Z. Chen, Theoretical analysis on the transient ignition of a premixed expanding flame in a quiescent mixture, J. Fluid Mech., 924 (2021) A22.

[29] D. Ren, X. Liu, X. Feng, L. Lu, M. Ouyang, J. Li, X. He. Model-based thermal runaway prediction of lithium-ion batteries from kinetics analysis of cell components, Appl. Energy 228 (2018) 633-644.

[30] B.J. Matkowsky, G.I. Sivashinsky, Propagation of a pulsating reaction front in solid fuel combustion, SIAM J. Appl. Math. 35 (1978) 465–478.